Available online at www.sciencedirect.com

SCIENCE DIRECT®

Journal of Computational Physics 212 (2006) 436–453

JOURNAL OF COMPUTATIONAL PHYSICS

www.elsevier.com/locate/jcp

A stable hybrid method for hyperbolic problems

Jan Nordström [a,b], Jing Gong [a,*]

[a] *Department of Information Technology, Scientific Computing, Uppsala University, P.O. Box 337, 75105 Uppsala, Sweden*
[b] *Department of Computational Physics, Division of Systems Technology, The Swedish Defence Research Agency, Stockholm, Sweden*

Received 23 September 2004; received in revised form 2 May 2005; accepted 7 July 2005
Available online 19 August 2005

Abstract

A stable hybrid method for hyperbolic problems that combines the unstructured finite volume method with high-order finite difference methods has been developed. The coupling procedure is based on energy estimates and stability can be guaranteed. Numerical calculations verify that the hybrid method is efficient and accurate.

Keywords: Hyperbolic problems; Hybrid methods; Finite difference; Finite volume; Coupling procedure; Stability; Efficiency

1. Introduction

The hyperbolic equations involved in modeling aerodynamic, aeroacoustic, or electromagnetic wave propagation remain a computational challenge both for academia and industry. In computational physics, unstructured finite volume methods are widely used to handle complex geometries and nonlinear phenomena. It is also clear that high-order finite difference methods are very efficient for essentially linear wave propagation problems in smooth geometries.

Strict stability, which prevents error growth on realistic mesh sizes, is very important for calculations over long times. Strictly stable unstructured finite volume methods and high-order finite difference methods for both hyperbolic, parabolic and incompletely parabolic problems were derived in [1–7]. These methods employ so called summation-by-parts (SBP) operators and impose the boundary conditions weakly, see [6,8].

In this paper, we will discuss how to combine the finite volume method and the high-order finite difference method into a hybrid method. The finite volume method will mainly be used close to the wave source,

* Corresponding author. Tel.: +46184716253.
E-mail addresses: jan.nordstrom@foi.se (J. Nordström), jing.gong@it.uu.se (J. Gong).

0021-9991/$ - see front matter
doi:10.1016/j.jcp.2005.07.008

where complex geometries and nonlinear phenomena are important, while the high-order finite difference method is ideally suited for the pure wave propagation part.

The coupling procedure will be based on energy estimates. Essentially, the whole procedure can be described as a way to modify the dual grid in the finite volume method in such a way that stability can be maintained at the interface. Examples of other types of hybrid methods and approaches can be found in [9–17].

Section 2 presents the two numerical methods and the coupling procedure. Section 3 deals with the numerical experiments, Section 4 discusses future extensions of the method and conclusions are drawn in Section 5.

2. Analysis

As a model problem, we will consider the continuous hyperbolic system

$$u_t + Au_x + Bu_y = 0, \qquad -1 \leqslant x \leqslant 1, \quad 0 \leqslant y \leqslant 1 \tag{1}$$

with suitable initial and boundary conditions. A and B are constant symmetric matrices with k rows and columns.

The computational domain will be divided into two subdomains. A so called edge-based unstructured finite volume method (UFVM) will be used to discretize (1) on subdomain $[-1,0] \times [0,1]$ with an unstructured mesh while a high-order finite difference method (HOFDM) will be used on subdomain $[0,1] \times [0,1]$ with a structured mesh, see Fig. 1.

The fact that the unknowns in the UFVM and the HOFDM are located in the nodes and can be co-located at the interface is a key ingredient in the coupling procedure we will discuss below.

2.1. The edge-based finite volume method

The computational domain consists of non-overlapping elements and the unknown variables are stored at the nodes of the mesh. For each node, the control volume that constitutes the dual grid is defined as a

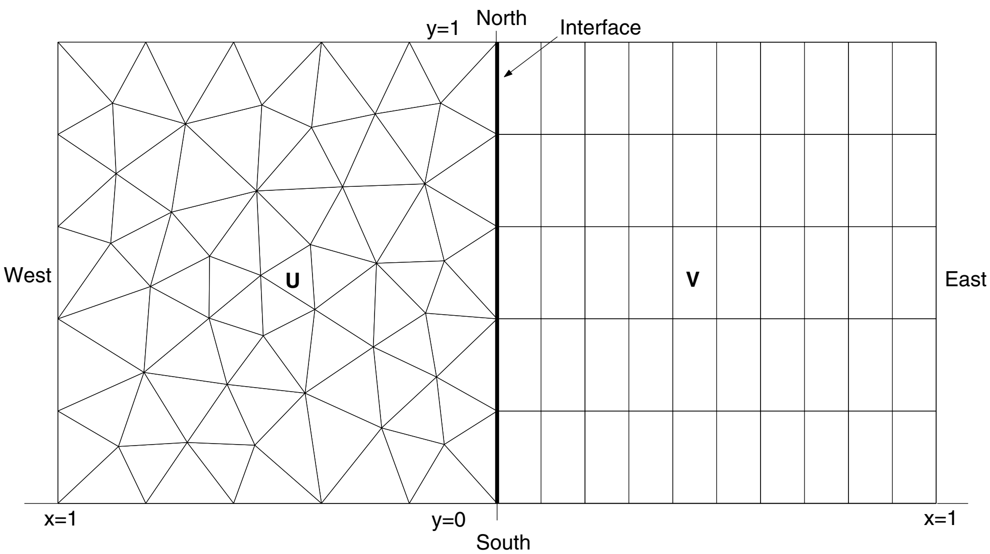

Fig. 1. The hybrid mesh on the computational domain.

polygon with its vertexes at the centers of gravity of the surrounding triangles (or quadrilaterals) and at the midpoints of the sides, see Fig. 2(a).

Eq. (1) is integrated over each control volume Ω_i, which is surrounded by the surface $\partial\Omega_i$ and we obtain,

$$\frac{\partial}{\partial t}\int\int_{\Omega_i} u\,\mathrm{d}x\,\mathrm{d}y + A\oint_{\partial\Omega_i} u\,\mathrm{d}y - B\oint_{\partial\Omega_i} u\,\mathrm{d}x = 0, \tag{2}$$

by Green's theorem.

In [6] it was shown that a semi-discrete approximation of Eq. (2) can be written,

$$(P^{\mathrm{L}}\otimes I_k)\mathbf{u}_t + (Q_x^{\mathrm{L}}\otimes A)\mathbf{u} + (Q_y^{\mathrm{L}}\otimes B)\mathbf{u} = 0, \tag{3}$$

or,

$$\mathbf{u}_t + \{[(P^{\mathrm{L}})^{-1}Q_x^{\mathrm{L}}]\otimes A\}\mathbf{u} + \{[(P^{\mathrm{L}})^{-1}Q_y^{\mathrm{L}}]\otimes B\}\mathbf{u} = 0, \tag{4}$$

where $\otimes$ is the Kronecker product. I_k is the $k\times k$ identity matrix. The discrete finite volume approximation of u at the nodes is denoted $\mathbf{u}$. It is a vector of length $M = mk$ where m is the number of nodes. The elements of $\mathbf{u}$ are arranged such that the first k elements are the discrete representation of the k variables in u at the first grid point. The following k elements are the discrete representation of the k variables in u at another grid point and so on. P^{L} is a positive diagonal $m\times m$ matrix with the control volumes Ω_i on the diagonal and Q_x^{L} and Q_y^{L} are almost skew-symmetric $m\times m$ matrices which represent the discrete approximation of the convective flux integral in (2).

The matrices Q_x^{L} and Q_y^{L} have the components:

$$(Q_x^{\mathrm{L}})_{ij} = \frac{\Delta y_j}{2} = -(Q_x^{\mathrm{L}})_{ji},\quad (Q_x^{\mathrm{L}})_{ii\notin\partial\Omega} = 0,\quad (Q_x^{\mathrm{L}})_{ii\in\partial\Omega} = \frac{\Delta y_i}{2}, \tag{5}$$

$$(Q_y^{\mathrm{L}})_{ij} = -\frac{\Delta x_j}{2} = -(Q_y^{\mathrm{L}})_{ji},\quad (Q_y^{\mathrm{L}})_{ii\notin\partial\Omega} = 0,\quad (Q_y^{\mathrm{L}})_{ii\in\partial\Omega} = -\frac{\Delta x_i}{2}. \tag{6}$$

For the definition of Δx_j and Δy_j, see Fig. 2. Moreover, Eqs. (5) and (6) imply that Q_x^{L} and Q_y^{R} satisfy

$$Q_x^{\mathrm{L}} + (Q_x^{\mathrm{L}})^{\mathrm{T}} = Y,\quad Q_y^{\mathrm{L}} + (Q_y^{\mathrm{L}})^{\mathrm{T}} = X, \tag{7}$$

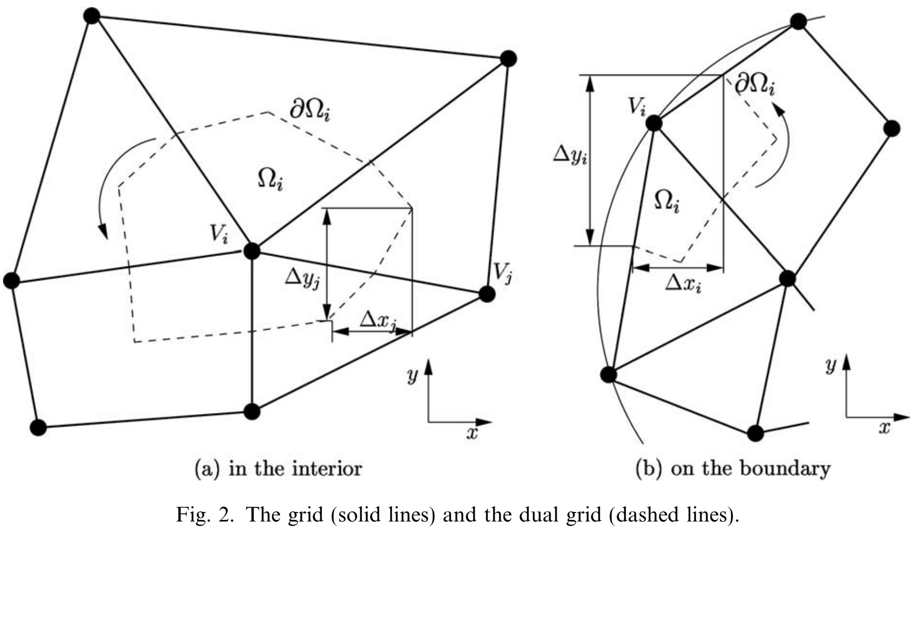

(a) in the interior (b) on the boundary

Fig. 2. The grid (solid lines) and the dual grid (dashed lines).

where the non-zero elements in Y and X are Δy_i and $-\Delta x_i$, respectively, and correspond to the boundary points.

The operators Q_x^{L} and Q_y^{L} satisfies a generalized SBP concept. By using (7) we obtain,

$$\phi^{\mathrm{T}} Y\phi = \sum_{i\in\partial\Omega} \phi_i^2 \Delta y_i \approx \oint_{\partial\Omega} \phi^2 \,\mathrm{d}y, \quad \phi^{\mathrm{T}} X\phi = -\sum_{i\in\partial\Omega} \phi_i^2 \Delta x_i \approx -\oint_{\partial\Omega} \phi^2 \,\mathrm{d}x, \tag{8}$$

where $\phi(x,y)$ is a smooth continuous function. For more details on the SBP properties of the finite volume scheme, see [6].

The finite volume scheme described above requires a particular boundary treatment to obtain stability. We will used the so called simultaneous approximation term (SAT) method where the boundary conditions are imposed weakly. The SAT technique is a penalty procedure that can be used to specify outer boundary conditions as well as treating block interfaces. We will not discuss the outer boundary treatment in detail, only indicate its presence by adding a penalty term on the right-hand side of (3). For more details on the weak treatment of boundary conditions, see [6].

The final semi-discrete form of (1) on subdomain $[-1,0]\times[0,1]$ can be written,

$$\mathbf{u}_t + \{[(P^{\mathrm{L}})^{-1} Q_x^{\mathrm{L}}] \otimes A\}\mathbf{u} + \{[(P^{\mathrm{L}})^{-1} Q_y^{\mathrm{L}}] \otimes B\}\mathbf{u} = \mathrm{SAT}^{\mathrm{L}} + \{[(P^{\mathrm{L}})^{-1}(E_I^{\mathrm{L}})^{\mathrm{T}} P_y^{\mathrm{L}}] \otimes \Sigma^{\mathrm{L}}\}(\mathbf{u}_I - \mathbf{v}_I), \tag{9}$$

where $\mathrm{SAT}^{\mathrm{L}}$ is the penalty term that imposes the outer boundary conditions weakly. $\mathbf{u}_I$ and $\mathbf{v}_I$ are vectors which represent $\mathbf{u}$ and $\mathbf{v}$ ($\mathbf{v}$ is the discrete finite difference solution that will be presented below) on the interface, respectively. E_I^{L} is a projection matrix which maps $\mathbf{u}$ to $\mathbf{u}_I$ such that $\mathbf{u}_I = (E_I^{\mathrm{L}} \otimes I_k)\mathbf{u}$. The non-zero components of E_I^{L} have the value 1 and appear at the interface. $P_y^{\mathrm{L}} \otimes \Sigma^{\mathrm{L}}$ is a penalty matrix that will be determined below by stability requirements.

Example. The precise structure of E_I^{L} depends on how $\mathbf{u}$ is organized. For unstructured grids, there are many different ways of doing that. If the first l elements of $\mathbf{u}$ are located on the interface, we obtain a projection matrix with the structure $E_I^{\mathrm{L}} = [I, 0]$ where E_I^{L} has dimension $l\times m$ and the identity matrix I has dimension $l\times l$.

2.2. *The high-order finite difference method*

Consider the subdomain $[0,1]\times[0,1]$ with a structured mesh of $n\times l$ points. The finite difference approximation of u at the grid point (x_i,y_j) is a $k\times 1$ vector denoted $\mathbf{v}_{ij}$. We organize the solution in the global vector $\mathbf{v} = [\mathbf{v}_{11},\ldots,\mathbf{v}_{1l},\mathbf{v}_{21},\ldots,\mathbf{v}_{2l},\ldots,\mathbf{v}_{n1},\ldots,\mathbf{v}_{nl}]^{\mathrm{T}}$. $\mathbf{v}_x$ and $\mathbf{v}_y$ are approximations of u_x and u_y and are approximated using the high-order accurate SBP operators for the first derivative that were constructed in [3,18,19]. The difference operators in the x and y direction on the right subdomain are denoted $(P_x^{\mathrm{R}})^{-1} Q_x^{\mathrm{R}}$ and $(P_y^{\mathrm{R}})^{-1} Q_y^{\mathrm{R}}$, respectively.

The semi-discrete approximation of (1) on subdomain $[0,1]\times[0,1]$ can be written,

$$\begin{aligned}
&\mathbf{v}_t + \left\{\left[\left(P_x^{\mathrm{R}}\right)^{-1} Q_x^{\mathrm{R}}\right] \otimes I_y^{\mathrm{R}} \otimes A\right\}\mathbf{v} + \left\{I_x^{\mathrm{R}} \otimes \left[\left(P_y^{\mathrm{R}}\right)^{-1} Q_y^{\mathrm{R}}\right] \otimes B\right\}\mathbf{v} \\
&\quad = \mathrm{SAT}^{\mathrm{R}} + \left\{\left[\left(P_x^{\mathrm{R}} \otimes P_y^{\mathrm{R}}\right)^{-1} (E_I^{\mathrm{R}})^{\mathrm{T}}\right] P_y^{\mathrm{R}} \otimes \Sigma^{\mathrm{R}}\right\}(\mathbf{v}_I - \mathbf{u}_I),
\end{aligned} \tag{10}$$

where the sizes of the identity matrices I_x^{R} and I_y^{R} are $n\times n$ and $l\times l$, respectively. $\mathrm{SAT}^{\mathrm{R}}$ is the SAT penalty term for the outer boundary conditions. E_I^{R} is a projection matrix which maps $\mathbf{v}$ to $\mathbf{v}_I$, that is, $\mathbf{v}_I = (E_I^{\mathrm{R}} \otimes I_k)\mathbf{v}$. Σ^{R} is a penalty matrix that will be determined below by stability requirements.

Example. With the organization of $\mathbf{v}$ given above we have $\mathbf{v}_I = [\mathbf{v}_{11},\ldots,\mathbf{v}_{1l}]^{\mathrm{T}}$ and consequently $E_I^{\mathrm{R}} = [I, 0]$, where E_I^{R} has dimension $1l \times nl$ and the identity matrix I has dimension $l \times l$.

Remark. Note that $\mathbf{u}_I$ and $\mathbf{v}_I$ in (9) and (10) are co-located at the interface. That is absolutely essential for the accuracy of the hybrid scheme. It will be shown below that it is also necessary for stability.

Note that the operators $(P_x^{\mathrm{R}})^{-1}Q_x^{\mathrm{R}}$ and $(P_y^{\mathrm{R}})^{-1}Q_y^{\mathrm{R}}$ are SBP operators since matrices P_x^{R} and P_y^{R} are symmetric and positive definite and the matrices Q_x and Q_y are nearly skew-symmetric, that is:

$$
\begin{aligned}
Q_x^{\mathrm{R}} + \left(Q_x^{\mathrm{R}}\right)^{\mathrm{T}} &= D_x^{\mathrm{R}} = \mathrm{diag}(-1, 0, \ldots 0, 1),\\
Q_y^{\mathrm{R}} + \left(Q_y^{\mathrm{R}}\right)^{\mathrm{T}} &= D_y^{\mathrm{R}} = \mathrm{diag}(-1, 0, \ldots 0, 1),
\end{aligned}
\tag{11}
$$

where D_x^{R} and D_y^{R} are $n \times n$ and $l \times l$ matrices, respectively.

In this paper, we will use the Kronecker product rules $(A \otimes B)(C \otimes D) = (AC) \otimes (BD)$ and $(A \otimes B)^{\mathrm{T}} = A^{\mathrm{T}} \otimes B^{\mathrm{T}}$. Applying these rules to the interface terms in (9) and (10) yields:

$$
\begin{aligned}
&\left\{\left[(P^{\mathrm{L}})^{-1}\left(E_I^{\mathrm{L}}\right)^{\mathrm{T}}P_y^{\mathrm{L}}\right] \otimes \Sigma^{\mathrm{L}}\right\} = [(P^{\mathrm{L}})^{-1} \otimes I_k]\left[\left(E_I^{\mathrm{L}}\right)^{\mathrm{T}} \otimes I_k\right]\left(P_y^{\mathrm{L}} \otimes \Sigma^{\mathrm{L}}\right),\\
&\left\{\left[\left(P_x^{\mathrm{R}} \otimes P_y^{\mathrm{R}}\right)^{-1}\left(E_I^{\mathrm{R}}\right)^{\mathrm{T}}P_y^{\mathrm{R}}\right] \otimes \Sigma^{\mathrm{R}}\right\} = \left[\left(P_x^{\mathrm{R}} \otimes P_y^{\mathrm{R}}\right)^{-1} \otimes I_k\right]\left[\left(E_I^{\mathrm{R}}\right)^{\mathrm{T}} \otimes I_k\right](P_y^{\mathrm{R}} \otimes \Sigma^{\mathrm{R}}).
\end{aligned}
$$

Note that the unknown penalty matrices above are P_y^{L}, Σ^{L}, and Σ^{R}. However, P_y^{R} is known.

2.3. Stable interface treatment

Define the norms $N^{\mathrm{L}} = P^{\mathrm{L}} \otimes I_k$ and $N^{\mathrm{R}} = (P_x^{\mathrm{R}} \otimes P_y^{\mathrm{R}}) \otimes I_k$, where $N^{\mathrm{L}} = (N^{\mathrm{L}})^{\mathrm{T}} > 0$ and $N^{\mathrm{R}} = (N^{\mathrm{R}})^{\mathrm{T}} > 0$. Moreover, define an inner product and a norm for discrete real vector-functions $\mathbf{a}, \mathbf{b} \in \mathbb{R}^n$ by

$$
(\mathbf{a}, \mathbf{b})_H = \mathbf{a}^{\mathrm{T}}H\mathbf{b}, \quad \|\mathbf{a}\|_H^2 = (\mathbf{a}, \mathbf{a}), \qquad H = H^{\mathrm{T}} > 0.
\tag{12}
$$

We apply the energy method by multiplying (9) and (10) with $\mathbf{u}^{\mathrm{T}}N^{\mathrm{L}}$ and $\mathbf{v}^{\mathrm{T}}N^{\mathrm{R}}$, respectively, which yields:

$$
\mathbf{u}^{\mathrm{T}}N^{\mathrm{L}}\mathbf{u}_t + \mathbf{u}^{\mathrm{T}}(Q_x^{\mathrm{L}} \otimes A)\mathbf{u} + \mathbf{u}^{\mathrm{T}}(Q_y^{\mathrm{L}} \otimes B)\mathbf{u} = \mathbf{u}^{\mathrm{T}}N^{\mathrm{L}} \cdot \mathrm{SAT}^{\mathrm{L}} + \mathbf{u}^{\mathrm{T}}[(E_I^{\mathrm{L}})^{\mathrm{T}} \otimes I_k](P_y^{\mathrm{L}} \otimes \Sigma^{\mathrm{L}})(\mathbf{u}_I - \mathbf{v}_I),
\tag{13}
$$

$$
\mathbf{v}^{\mathrm{T}}N^{\mathrm{R}}\mathbf{v}_t + \mathbf{v}^{\mathrm{T}}(Q_x^{\mathrm{R}} \otimes P_y^{\mathrm{R}} \otimes A)\mathbf{v} + \mathbf{v}^{\mathrm{T}}(P_x^{\mathrm{R}} \otimes Q_y^{\mathrm{R}} \otimes B)\mathbf{v} = \mathbf{v}^{\mathrm{T}}N^{\mathrm{R}} \cdot \mathrm{SAT}^{\mathrm{R}} + \mathbf{v}^{\mathrm{T}}[(E_I^{\mathrm{R}})^{\mathrm{T}} \otimes I_k](P_y^{\mathrm{R}} \otimes \Sigma^{\mathrm{R}})(\mathbf{v}_I - \mathbf{u}_I).
\tag{14}
$$

By adding the transposes of (13) and (14), and using (7), (11), and (12) we get:

$$
\begin{aligned}
\frac{\mathrm{d}}{\mathrm{d}t}(\|\mathbf{u}\|_{N^{\mathrm{L}}}^2) = {} & -\mathbf{u}^{\mathrm{T}}(Y \otimes A)\mathbf{u} - \mathbf{u}^{\mathrm{T}}(X \otimes B)\mathbf{u} + 2\mathbf{u}^{\mathrm{T}}N^{\mathrm{L}} \cdot \mathrm{SAT}^{\mathrm{L}} + \mathbf{u}^{\mathrm{T}}\left[\left(E_I^{\mathrm{L}}\right)^{\mathrm{T}} \otimes I_k\right]\left(P_y^{\mathrm{L}} \otimes \Sigma^{\mathrm{L}}\right)(\mathbf{u}_I - \mathbf{v}_I)\\
& + (\mathbf{u}_I - \mathbf{v}_I)^{\mathrm{T}}\left(P_y^{\mathrm{L}} \otimes \Sigma^{\mathrm{L}}\right)^{\mathrm{T}}\left[\left(E_I^{\mathrm{L}}\right)^{\mathrm{T}} \otimes I_k\right]^{\mathrm{T}}\mathbf{u},
\end{aligned}
\tag{15}
$$

$$
\begin{aligned}
\frac{\mathrm{d}}{\mathrm{d}t}(\|\mathbf{v}\|_{N^{\mathrm{R}}}^2) = {} & -\mathbf{v}^{\mathrm{T}}\left(D_x^{\mathrm{R}} \otimes P_y^{\mathrm{R}} \otimes A\right)\mathbf{v} - \mathbf{v}^{\mathrm{T}}\left(P_x^{\mathrm{R}} \otimes D_y^{\mathrm{R}} \otimes B\right)\mathbf{v} + 2\mathbf{v}^{\mathrm{T}}N^{\mathrm{R}} \cdot \mathrm{SAT}^{\mathrm{R}}\\
& + \mathbf{v}^{\mathrm{T}}\left[\left(E_I^{\mathrm{R}}\right)^{\mathrm{T}} \otimes I_k\right]\left(P_y^{\mathrm{R}} \otimes \Sigma^{\mathrm{R}}\right)(\mathbf{v}_I - \mathbf{u}_I) + (\mathbf{v}_I - \mathbf{u}_I)^{\mathrm{T}}\left(P_y^{\mathrm{R}} \otimes \Sigma^{\mathrm{R}}\right)^{\mathrm{T}}\left[\left(E_I^{\mathrm{R}}\right)^{\mathrm{T}} \otimes I_k\right]^{\mathrm{T}}\mathbf{v}.
\end{aligned}
\tag{16}
$$

In (15), we will use the relation (8) that leads to:

$$\phi^{\mathrm{T}} Y \phi = \sum_{i \in \partial\Omega/\mathrm{Interface}} \phi_i^2 \Delta y_i + \sum_{i \in \mathrm{Interface}} \phi_i^2 \Delta y_i = \phi_B^{\mathrm{T}} P_y^B \phi_B + \phi_I^{\mathrm{T}} P_y^{\mathrm{L}} \phi_I, \tag{17}$$

$$\phi^{\mathrm{T}} X \phi = -\sum_{i \in \partial\Omega/\mathrm{Interface}} \phi_i^2 \Delta x_i + \sum_{i \in \mathrm{Interface}} \phi_i^2 \Delta x_i = \phi_B^{\mathrm{T}} P_x^B \phi_B + \phi_I^{\mathrm{T}} P_x^{\mathrm{L}} \phi_I, \tag{18}$$

where ϕ_B and ϕ_I are vectors located at the boundary and interface points, respectively. It is obvious that P_x^B, P_y^B, P_x^{L}, and P_y^{L} are diagonal matrices.

Recall that $((E_I^{\mathrm{L}})^{\mathrm{T}} \otimes I_k)^{\mathrm{T}} = E_I^{\mathrm{L}} \otimes I_k$ and $(E_I^{\mathrm{L}})^{\mathrm{T}} \otimes I_k = (E_I^{\mathrm{L}} \otimes I_k)^{\mathrm{T}}$ since I_k is the identity matrix. The terms in (15) can be written:

$$\begin{aligned}
&\mathbf{u}^{\mathrm{T}}(Y \otimes A)\mathbf{u} = \mathbf{u}_B^{\mathrm{T}}\left(P_y^B \otimes A\right)\mathbf{u}_B + \mathbf{u}_I^{\mathrm{T}}\left(P_y^{\mathrm{L}} \otimes A\right)\mathbf{u}_I,\\
&\mathbf{u}^{\mathrm{T}}(X \otimes B)\mathbf{u} = \mathbf{u}_B^{\mathrm{T}}\left(P_x^B \otimes B\right)\mathbf{u}_B + \mathbf{u}_I^{\mathrm{T}}\left(P_x^{\mathrm{L}} \otimes B\right)\mathbf{u}_I,\\
&\mathbf{u}^{\mathrm{T}}\left[\left(E_I^{\mathrm{L}}\right)^{\mathrm{T}} \otimes I_k\right]\left(P_y^{\mathrm{L}} \otimes \Sigma^{\mathrm{L}}\right)(\mathbf{u}_I - \mathbf{v}_I) = \mathbf{u}_I^{\mathrm{T}}\left(P_y^{\mathrm{L}} \otimes \Sigma^{\mathrm{L}}\right)(\mathbf{u}_I - \mathbf{v}_I),\\
&(\mathbf{u}_I - \mathbf{v}_I)^{\mathrm{T}}(P_y^{\mathrm{L}} \otimes \Sigma^{\mathrm{L}})^{\mathrm{T}}[(E_I^{\mathrm{L}})^{\mathrm{T}} \otimes I_k]^{\mathrm{T}}\mathbf{u} = (\mathbf{u}_I - \mathbf{v}_I)^{\mathrm{T}}[P_y^{\mathrm{L}} \otimes (\Sigma^{\mathrm{L}})^{\mathrm{T}}]\mathbf{u}_I.
\end{aligned} \tag{19}$$

The terms at the right-hand side of (16) can be written:

$$\begin{aligned}
&\mathbf{v}^{\mathrm{T}}\left(D_x^{\mathrm{R}} \otimes P_y^{\mathrm{R}} \otimes A\right)\mathbf{v} = -\mathbf{v}_I^{\mathrm{T}}\left(P_y^{\mathrm{R}} \otimes A\right)\mathbf{v}_I + \mathbf{v}_E^{\mathrm{T}}\left(P_y^{\mathrm{R}} \otimes A\right)\mathbf{v}_E,\\
&\mathbf{v}^{\mathrm{T}}\left(P_x^{\mathrm{R}} \otimes D_y^{\mathrm{R}} \otimes B\right)\mathbf{v} = -\mathbf{v}_S^{\mathrm{T}}\left(P_y^{\mathrm{R}} \otimes B\right)\mathbf{v}_S + \mathbf{v}_N^{\mathrm{T}}\left(P_y^{\mathrm{R}} \otimes B\right)\mathbf{v}_N,\\
&\mathbf{v}^{\mathrm{T}}\left[\left(E_I^{\mathrm{R}}\right)^{\mathrm{T}} \otimes I_k\right]\left(P_y^{\mathrm{R}} \otimes \Sigma^{\mathrm{R}}\right)(\mathbf{v}_I - \mathbf{u}_I) = \mathbf{v}_I^{\mathrm{T}}\left(P_y^{\mathrm{R}} \otimes \Sigma^{\mathrm{R}}\right)(\mathbf{v}_I - \mathbf{u}_I),\\
&(\mathbf{v}_I - \mathbf{u}_I)^{\mathrm{T}}\left(P_y^{\mathrm{R}} \otimes \Sigma^{\mathrm{R}}\right)^{\mathrm{T}}\left[\left(E_I^{\mathrm{R}}\right)^{\mathrm{T}} \otimes I_k\right]^{\mathrm{T}}\mathbf{v} = (\mathbf{v}_I - \mathbf{u}_I)^{\mathrm{T}}\left[P_y^{\mathrm{R}} \otimes (\Sigma^{\mathrm{R}})^{\mathrm{T}}\right]\mathbf{v}_I,
\end{aligned} \tag{20}$$

where $\mathbf{v}_E$, $\mathbf{v}_S$, $\mathbf{v}_N$ denote the solution on the east, south and north boundaries (see Fig. 1).

In the following we assume that the terms including $\mathbf{u}_B$, $\mathbf{v}_E$, $\mathbf{v}_S$, $\mathbf{v}_N$ at the outer boundaries are precisely cancelled by the SAT terms (see [2,5,20]). Note that $P_x^{\mathrm{L}} = 0$ since $\Delta x_i = 0$ at the interface and that P_y^{L} and P_y^{R} are diagonal matrices of the same size.

By using (19) and (20), the energy estimate becomes

$$\frac{\mathrm{d}}{\mathrm{d}t}\left(\|u\|_{N^{\mathrm{L}}}^2 + \|u\|_{N^{\mathrm{R}}}^2\right) = [\mathbf{u}_I, \mathbf{v}_I]^{\mathrm{T}} M_I [\mathbf{u}_I, \mathbf{v}_I], \tag{21}$$

where

$$M_I = \begin{bmatrix} -P_y^{\mathrm{L}} \otimes A + P_y^{\mathrm{L}} \otimes \Sigma^{\mathrm{L}} + P_y^{\mathrm{L}} \otimes (\Sigma^{\mathrm{L}})^{\mathrm{T}} & -P_y^{\mathrm{L}} \otimes \Sigma^{\mathrm{L}} - P_y^{\mathrm{R}} \otimes \Sigma^{\mathrm{R}} \\ -P_y^{\mathrm{L}} \otimes \Sigma^{\mathrm{L}} - P_y^{\mathrm{R}} \otimes \Sigma^{\mathrm{R}} & P_y^{\mathrm{R}} \otimes A + P_y^{\mathrm{R}} \otimes \Sigma^{\mathrm{R}} + P_y^{\mathrm{R}} \otimes (\Sigma^{\mathrm{R}})^{\mathrm{T}} \end{bmatrix}.$$

We need M_I to be negative semi-definite for stability. Consider a simplified case where,

$$P_y^{\mathrm{L}} = P_y^{\mathrm{R}} = P_y, \quad \Sigma^{\mathrm{L}} = (\Sigma^{\mathrm{L}})^{\mathrm{T}}, \quad \Sigma^{\mathrm{R}} = (\Sigma^{\mathrm{R}})^{\mathrm{T}}. \tag{22}$$

This yields

$$M_I = P_y \otimes \begin{bmatrix} -A + 2\Sigma^{\mathrm{L}} & -\Sigma^{\mathrm{L}} - \Sigma^{\mathrm{R}} \\ -\Sigma^{\mathrm{L}} - \Sigma^{\mathrm{R}} & A + 2\Sigma^{\mathrm{R}} \end{bmatrix} = P_y \otimes M.$$

To obtain stability M has to be negative semi-definite. We can diagonalize A by $X^{\mathrm{T}} A X = \Lambda$, where X is an orthogonal matrix consisting of the eigenvectors of A. Moreover, consider penalty parameters Σ^{L} and Σ^{R} of the form $X^T\Sigma^L X = \Lambda^L$ and $X^T\Sigma^R X = \Lambda^R$. Denote by λ_i the ith diagonal component of Λ and similarly λ_i^L and λ_i^R for Λ^L and Λ^R. Then we obtain a negative semi-definite M if:

$$\lambda_i^R = \lambda_i^L - \lambda_i, \tag{23}$$

$$\lambda_i^L \leqslant \frac{\lambda_i}{2} \tag{24}$$

for $i = 1,\ldots,k$.

Remark. Eq. (23) is recognized as the condition for a conservative interface treatment. The condition (24) leads to stability if conservation is guaranteed via (23). For more details, see [5,20].

We have proved the following proposition,

Proposition 2.1. *If the conditions (22)–(24) hold, (21) leads to a bounded energy and (9), (10) have a stable and conservative interface treatment.*

We can also prove,

Proposition 2.2. *The eigenvalues of M are $2(2\lambda_i^L - \lambda_i)$ $(i = 1,\ldots,k)$ and k duplicative zeros.*

Proof. Inserting $\Sigma^L = X\Lambda^L X^T$ and $\Sigma^R = X\Lambda^R X^T = X(\Lambda^L - \Lambda)X^T$ into matrix M, we have

$$\begin{aligned} M &= \begin{bmatrix} X(2\Lambda^L - \Lambda)X^T & -X(2\Lambda^L - \Lambda)X^T \\ -X(2\Lambda^L - \Lambda)X^T & X(2\Lambda^L - \Lambda)X^T \end{bmatrix} = X(2\Lambda^L - \Lambda)X^T \otimes \begin{bmatrix} 1 & -1 \\ -1 & 1 \end{bmatrix} \\ &= X(2\Lambda^L - \Lambda)X^T \otimes \left\{ \begin{bmatrix} -\frac{1}{\sqrt{2}} & -\frac{1}{\sqrt{2}} \\ -\frac{1}{\sqrt{2}} & \frac{1}{\sqrt{2}} \end{bmatrix} \begin{bmatrix} 0 & 0 \\ 0 & 2 \end{bmatrix} \begin{bmatrix} -\frac{1}{\sqrt{2}} & -\frac{1}{\sqrt{2}} \\ -\frac{1}{\sqrt{2}} & \frac{1}{\sqrt{2}} \end{bmatrix} \right\} \\ &= \left\{ X \otimes \begin{bmatrix} -\frac{1}{\sqrt{2}} & -\frac{1}{\sqrt{2}} \\ -\frac{1}{\sqrt{2}} & \frac{1}{\sqrt{2}} \end{bmatrix} \right\} \left\{ (2\Lambda^L - \Lambda) \otimes \begin{bmatrix} 0 & 0 \\ 0 & 2 \end{bmatrix} \right\} \left\{ X^T \otimes \begin{bmatrix} -\frac{1}{\sqrt{2}} & -\frac{1}{\sqrt{2}} \\ -\frac{1}{\sqrt{2}} & \frac{1}{\sqrt{2}} \end{bmatrix} \right\} \\ &= X_M \Lambda_M X_M^T, \quad X_M = X \otimes \begin{bmatrix} -\frac{1}{\sqrt{2}} & -\frac{1}{\sqrt{2}} \\ -\frac{1}{\sqrt{2}} & \frac{1}{\sqrt{2}} \end{bmatrix}, \quad \Lambda_M = \begin{bmatrix} 0_k & 0_k \\ 0_k & 2(2\Lambda^L - \Lambda) \end{bmatrix}. \end{aligned}$$

In the equation above, 0_k is an $k \times k$ matrix of zeros, X_M is the matrix consisting of the eigenvectors of M and Λ_M is the diagonal matrix of eigenvalues of M. Hence the eigenvalues of matrix M are $2(2\lambda_i^L - \lambda_i)$ $(i = 1,\ldots,k)$ and k duplicative zeros. $\square$

Remark. If (23) holds, the maximal eigenvalue of M is zero, i.e., M is negative semi-definite.

The specific SBP operators that are based on diagonal norms are given in [3,19]. When we use the second-order diagonal norm $P_y^R = \mathrm{diag}[1/2, 1, \ldots, 1, 1/2]/h$ on the right subdomain, we do not need to change the control volume since $P_y^L = P_y^R$. But the standard fourth- and sixth-order diagonal norms are

$$\frac{1}{h}\begin{bmatrix} \frac{17}{48} & & & & & \\ & \frac{59}{48} & & & & \\ & & \frac{43}{48} & & & \\ & & & \frac{49}{48} & & \\ & & & & 1 & \\ & & & & & \ddots \end{bmatrix}, \quad \frac{1}{h}\begin{bmatrix} \frac{13649}{43200} & & & & & & & \\ & \frac{12013}{8640} & & & & & & \\ & & \frac{2711}{4320} & & & & & \\ & & & \frac{5359}{4320} & & & & \\ & & & & \frac{7877}{8640} & & & \\ & & & & & \frac{43801}{43200} & & \\ & & & & & & 1 & \\ & & & & & & & \ddots \end{bmatrix}, \tag{25}$$

respectively. In both cases, we need to modify the control volume for the UFVM at the points on the interface to guarantee $P_y^L = P_y^R$. The old dual grid for the points at the interface consists of the lines between

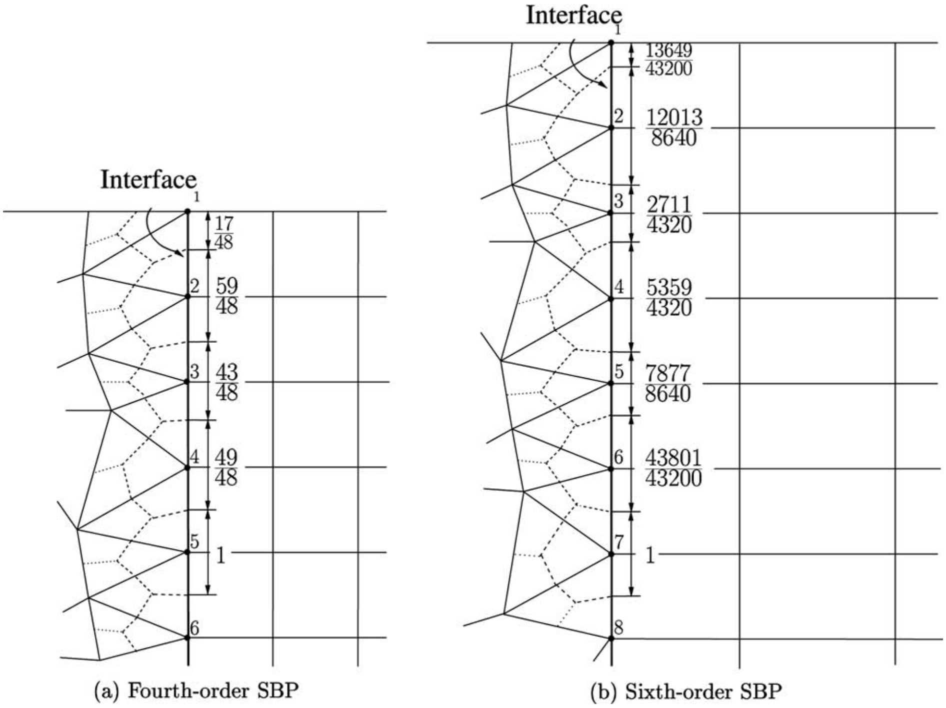

Fig. 3. The modified control volumes for the points on the interface.

the center of the triangles and the midpoints of the edges. In order to match P_y^{L} and P_y^{R}, the new lines will connect the center of the triangles and the points at the interface which correspond to the P_y^{R}, see Fig. 3.

3. Numerical experiments

Consider the scalar advection equation,

$$u_t + au_x + bu_y = 0, \qquad -1 \leqslant x \leqslant 1,\ 0 \leqslant y \leqslant 1, \quad b > 0, \tag{26}$$

where the exact solution is $u(x,y,t) = f(x,y,t) = \sin(2\pi(x/a + y/b - 2t))$. As initial data, we use $u(x,y,0) = f(x,y,0)$. For $a > 0$, we use the boundary conditions $u(x,0,t) = f(x,0,t)$, $u(-1,y,t) = f(-1,y,t)$, while we replace $u(-1,y,t) = f(-1,y,t)$ with $u(1,y,t) = f(1,y,t)$ for $a < 0$.

The problem (26) is a special case of the hyperbolic system we analyzed above. However, the main difficulties are the same; namely to get the accuracy by co-locating points on the interface and stability by choosing the finite volume norm and penalty parameters correctly.

3.1. Eigenvalue analysis

By the previous analysis we know that the long-time behavior for the hybrid method is determined by the eigenvalues of interface matrix M. Consider a case where the left subdomain has an unstructured mesh with 704 nodes and the right subdomain has a structured mesh with 21×21 grid points (see Fig. 1). The

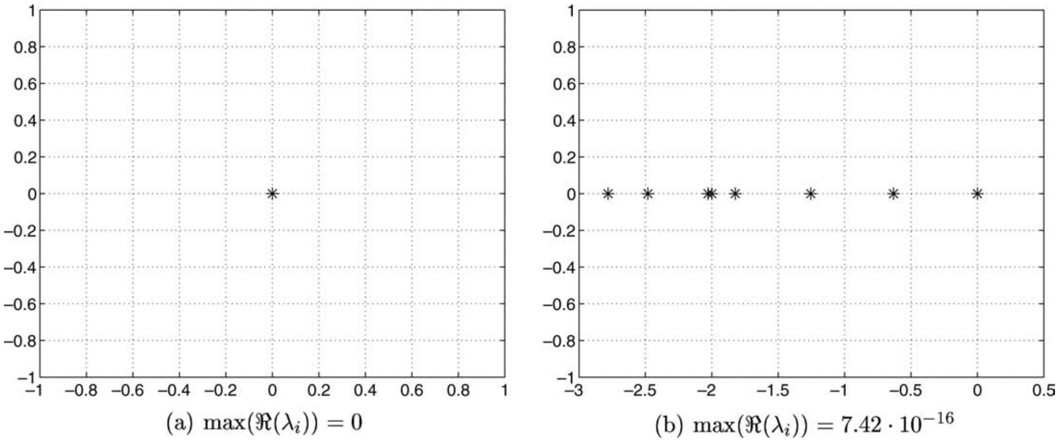

Fig. 4. Spectra of the interface matrix M. (a) $P_y^{\mathrm{L}} = P_y^{\mathrm{R}}$, $\Sigma^{\mathrm{L}} = 1/2$ and $\Sigma^{\mathrm{R}} = -1/2$; (b) $P_y^{\mathrm{L}} = P_y^{\mathrm{R}}$, $\Sigma^{\mathrm{L}} = 0$ and $\Sigma^{\mathrm{R}} = -1$.

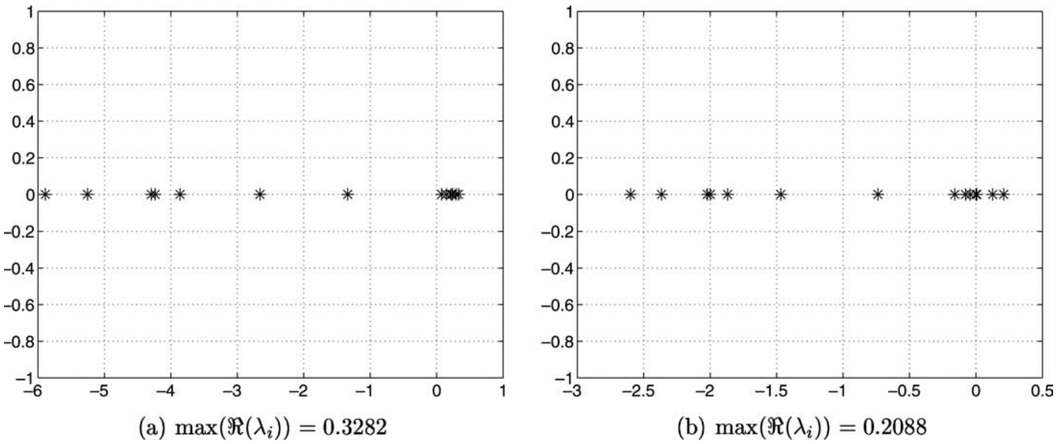

Fig. 5. Spectra of the interface matrix M. (a) $P_y^{\mathrm{L}} = P_y^{\mathrm{R}}$, $\Sigma^{\mathrm{L}} = 0$ and $\Sigma^{\mathrm{R}} = -2$; (b) $P_y^{\mathrm{L}} \neq P_y^{\mathrm{R}}$, $\Sigma^{\mathrm{L}} = 0$ and $\Sigma^{\mathrm{R}} = -1$.

HOFDM with the sixth-order SBP operator is used on the right subdomain. Let $a = 1$, $b = 2$ and $P_y^{\mathrm{L}} = P_y^{\mathrm{R}}$. We consider two cases: $\Sigma^{\mathrm{L}} = 1/2$, $\Sigma^{\mathrm{R}} = -1/2$ and $\Sigma^{\mathrm{L}} = 0$, $\Sigma^{\mathrm{R}} = -1$. For both cases, (22)–(24) are satisfied. In Fig. 4, we can see that all eigenvalues are located in the left half of the complex plane (including the zero eigenvalues). However, if one or more of the stability conditions cannot be guaranteed, some of eigenvalues might get positive real parts (see Fig. 5). These eigenvalues will lead to exponential time-growth and (unless they are of $\mathcal{O}(h)$) an unstable scheme.

3.2. One domain calculation

In this section, we test how efficient and accurate the high-order SBP operator is on one domain. We start by defining the rate of convergence, q, on the computational domain as

$$q = \frac{\log_{10}\left(\|u - v^{(1)}\|_2 / \|u - v^{(2)}\|_2\right)}{\log_{10}\left(\sqrt{N^{(1)}}/\sqrt{N^{(2)}}\right)},$$

where u is the exact solution. $v^{(1)}$ and $v^{(2)}$ are the corresponding numerical solutions on meshes with $N^{(1)}$ and $N^{(2)}$ nodes (including boundary nodes), respectively.

The convergence rate for both HOFDM and UFVM on one domain are displayed in Table 1. The structured mesh is refined from 861 to 125,751 nodes. We use the classical fourth-order Runge–Kutta method for the time integration. A small time-step is used to minimize the temporal errors.

The convergence rates for the second-, fourth- and sixth-order schemes are 2, 3 and 4, respectively. Those results are in line with the theory in [21–23], since we use diagonal norms that lead to first-, second- and third-order accuracy at the boundaries. The convergence rate for the UFVM is 2 on the structured symmetric mesh. One can prove that the UFVM is at least first-order accurate on a general triangular mesh.

The UFVM requires 5 flops at an edge that connects two nodes for the computation of a gradient in two dimensions. On a cartesian mesh, the number of edges are twice the number of nodes which means that $10 + 10 + 1 = 21$ flops are required for the computation of the sum of the x and y gradients at a node point. The second-, fourth- and sixth-order finite difference method requires $3 + 3 + 1 = 7$, $6 + 6 + 1 = 13$ and $9 + 9 + 1 = 19$ flops for the same task.

Note that $\log(L_2 - \text{error})$ is -2.64 for the UFVM scheme on a fine mesh of 29,161 nodes and approximately -2.66 for the fourth- and sixth-order HOFDM on a coarse mesh of 861 nodes. The second-order finite difference scheme has a $\log(L_2 - \text{error})$ of -2.61 for 7381 nodes. The operation count above implies that all the HOFDMs are more accurate and efficient than the UFVM. For high accuracy requirements, the sixth-order method is of course the most efficient.

Figs. 6 and 7 show the results for HOFDM with sixth-order SBP operator at $T = 1$ on one domain. The calculations have a $\log(L_2 - \text{error})$ of -2.67 on a mesh with 861 nodes and -3.84 on a mesh with 3321 nodes. On the same mesh, the numerical solution for the UFVM is displayed in Fig. 8. Note the significant difference in error levels.

3.3. Two subdomains with an interface

Next, we will illustrate the efficiency of the hybrid method. We calculate on two subdomains with an interface at $x = 0$. First, we apply the UFVM on an unstructured mesh in both subdomains. Next, we use the UFVM on the same mesh in the left subdomain and the HOFDM on a structured mesh in the right subdomain. Finally, we reduce the number of grid points in the right subdomain until we obtain a similar L_2 – error in both subdomains.

The mesh enlargement is done in the x-direction only and Δy is kept constant. As previously shown, stability and accuracy require that the finite volume and finite difference solutions are co-located at the interface.

Table 1
Convergence rates of approximations to $u_t + u_x + 2u_y = 0$ on one domain

Nodes	HOFDM (2nd)		HOFDM (4th)		HOFDM (6th)		UFVM	
	Error	q	Error	q	Error	q	Error	q
861	−1.65		−2.66		−2.67		−1.06	
3321	−2.26	2.07	−3.59	3.17	−3.84	4.00	−1.69	2.13
7381	−2.61	2.03	−4.13	3.09	−4.55	4.12	−2.04	2.05
13,041	−2.86	2.02	−4.51	3.06	−5.06	4.11	−2.29	2.02
20,301	−3.06	2.02	−4.80	3.06	−5.46	4.11	−2.49	2.02
29,161	−3.21	2.01	−5.04	3.02	−5.78	4.05	−2.64	2.00
37,950	−3.33	2.03	−5.21	2.98	−6.01	4.05	−2.75	1.91
125,751	−3.85	2.01	−6.00	3.02	−7.07	4.06	−3.27	1.99

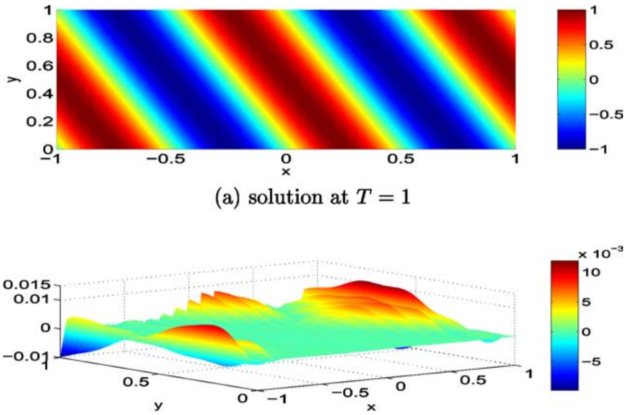

(a) solution at $T = 1$

(b) error at $T = 1$

Fig. 6. HOFDM with sixth-order SBP operators used on the whole computational domain with 861 nodes and $\log(L_2 - \text{error}) = -2.67$.

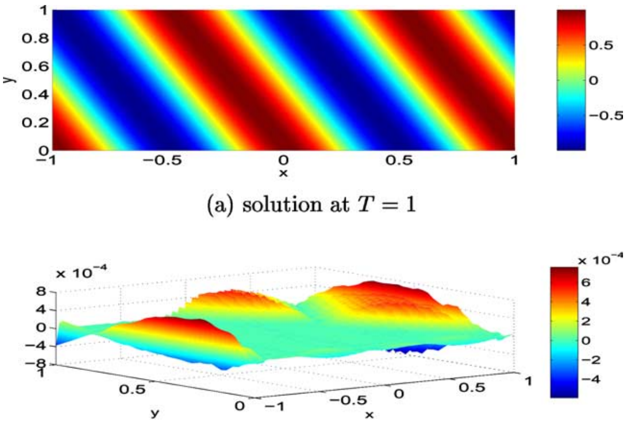

(a) solution at $T = 1$

(b) error at $T = 1$

Fig. 7. HOFDM with sixth-order SBP operators used on the whole computational domain with 3321 nodes and $\log(L_2 - \text{error}) = -3.84$.

Table 2 shows that the rate of convergence for the UFVM is less than 2 on unstructured, unsymmetrical meshes. The $\log(L_2 - \text{error})$ is -3.16 for UFVM scheme on the finest mesh with 138,113 nodes. To obtain the same error level we need a mesh with 93,447 and 79,377 nodes for the two hybrid methods, respectively. We can also see that in the sixth-order case only one sixth of the nodes are required for the HOFDM.

In the calculations shown in Fig. 9, we have used 2807 grid points in the left subdomain and 861 in the right subdomain. The major part of the error in Fig. 9 is created in the left domain (with the fine mesh and low accuracy) and advected into the right domain (with the coarse mesh and high accuracy).

In the previous calculations, the left subdomain with the unstructured mesh can be considered a modelling the source field while the right subdomain with the structured mesh can be considered as the wave propagation domain. The previous numerical results illustrate the efficiency of the hybrid method when waves propagate from the source to the far field.

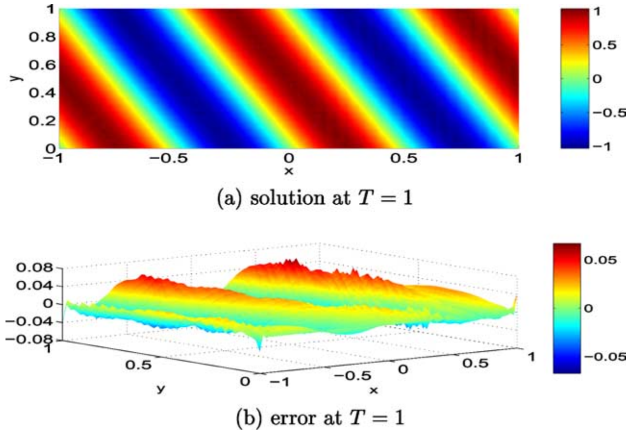

Fig. 8. UFVM used on the whole computational domain with 3321 nodes and $\log(L_2 - \text{error}) = -1.69$.

Table 2
Convergence rates of approximations to $u_t + u_x + 2u_y = 0$ on two subdomains

UFVM (whole domain)			Hybrid (UFVM + HOFDM (2nd))			Hybrid (UFVM + HOFDM (6th))		
Nodes	Error	q	Nodes	Error	q	Nodes	Error	q
1410	−1.39		1145 (704 + 441)	−1.34		1019 (704 + 315)	−1.36	
5569	−1.94	1.84	4488 (2807 + 1681)	−1.91	1.92	3396 (2807 + 1189)	−1.94	1.96
22,331	−2.49	1.82	17,700 (11,139 + 6561)	−2.47	1.88	14,460 (11,139 + 3321)	−2.48	1.93
78,543	−2.97	1.76	54,370 (39,119 + 15,251)	−2.98	2.09	46,820 (39,119 + 7701)	−2.98	1.96
138,113	−3.16	1.56	93,447 (69,126 + 24,321)	−3.16	1.54	79,377 (69,126 + 10,251)	−3.16	1.57

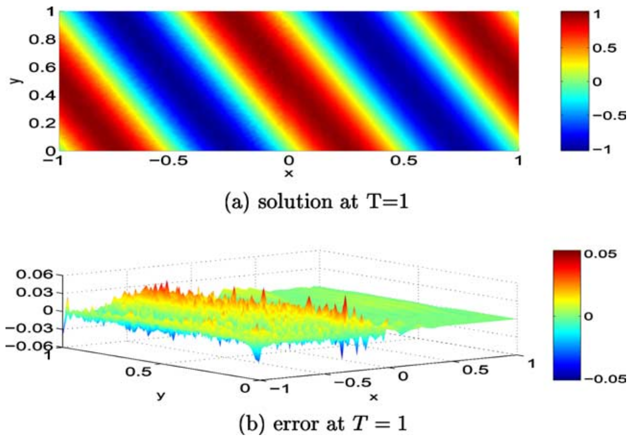

Fig. 9. $\log(L_2 - \text{error}) = -1.87$ on the left domain with 2807 nodes and $\log(L_2 - \text{error}) = -2.22$ on the right domain with 861 nodes for $u_t + u_x + 2u_y = 0$.

It is also of interest to investigate the efficiency of the method for waves propagating from the far field to the source. To illustrate this, consider equation $u_t - u_x + 2u_y = 0$ with initial and boundary conditions as described below Eq. (26).

The calculations are shown in Fig. 10. We obtain similar error levels as we did for the previous case on coarse meshes (see Table 3). However, for fine meshes, only one eleventh of the nodes are used for the HOFDM in the sixth-order case. This implies that the efficiency of the hybrid method is even better in this case.

The hybrid method is intended for problems where one needs the UFVM in a relatively small part of the computational domain. To estimate the efficiency of the hybrid method we therefore consider a case with one domain (of unit size) where UFVM is used is coupled in the x-direction to l such unit domains where HOFDM is used (see Fig. 13 below). We compare that calculation with a case where UFVM is used on the whole ($l+1$ unit domains large) computational domain. We estimate the efficiency for large l as

$$\text{Efficiency} = \lim_{l\to\infty} \frac{l \times N_{\text{HOFDM}} + N_{\text{UFVM}}}{(l+1) \times N_{\text{UFVM}}} = \frac{N_{\text{HOFDM}}}{N_{\text{UFVM}}}, \tag{27}$$

where N_{HOFDM} and N_{UFVM} denote the number of flops for the finite difference and finite volume calculation, respectively.

For a triangular mesh, the number of edges are three times the number of nodes. This means that $15+15+1=31$ flops per node are required for the UFVM computation of the sum of the x and y gradients. As mentioned above, the second-order and sixth-order finite difference methods require 7 and 19 flops, respectively, for the same task.

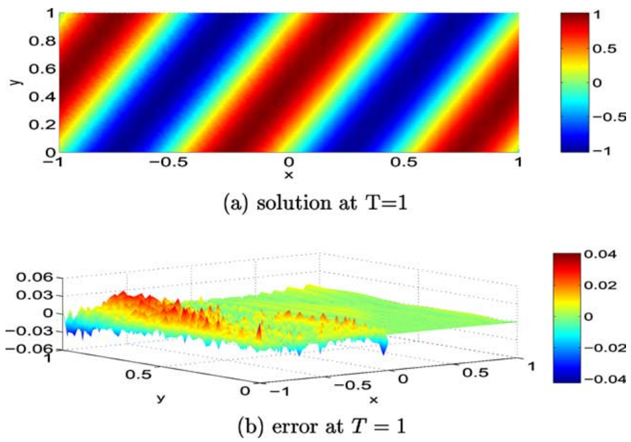

Fig. 10. $\log(L_2 - \text{error}) = -1.98$ on the left subdomain with 2807 nodes and $\log(L_2 - \text{error}) = -2.42$ on the right subdomain with 861 nodes for $u_t - u_x + 2u_y = 0$.

Table 3
Convergence rates for approximations to $u_t - u_x + 2u_y = 0$ on two subdomains

UFVM (whole domain)			Hybrid (UFVM + HOFDM (2nd))			Hybrid (UFVM + HOFDM (6th))		
Nodes	Error	q	Nodes	Error	q	Nodes	Error	q
1410	−1.36		1019 (704 + 315)	−1.35		977 (704 + 273)	−1.43	
5569	−1.96	2.01	4078 (2807 + 1271)	−1.96	2.02	3422 (2807 + 615)	−1.94	1.87
22,331	−2.49	1.76	15,270 (11,139 + 4131)	−2.47	1.78	12,840 (11,139 + 1701)	−2.50	1.95
78,543	−2.96	1.72	51,350 (39,119 + 12,231)	−2.97	1.90	43,800 (39,119 + 4681)	−2.97	1.76
138,113	−3.15	1.58	92,241 (69,126 + 23,115)	−3.15	1.43	75,357 (69,126 + 6231)	−3.15	1.57

In Figs. 11 and 12, we can see the result where we for simplicity have used the data (number of flops) from Tables 2 and 3, respectively. Both hybrid methods are more efficient than the UFVM method. Due to the low operation count, the hybrid using the second-order finite difference method is very efficient. For a vanishing grid-size, the hybrid using the sixth-order finite difference method will be the most efficient choice.

Note that the efficiency gain discussed above is almost "one-dimensional" due to the mesh refinement in the x-direction only. That limitation is due to the fact that we need co-located nodes at the interface. For a more multi-dimensional case (which will appear in most applications), for example with the UFVM in a convex domain surrounded by a structured mesh, even more efficiency can be gained.

Next, we consider the hybrid method on the large domain $[-1,10] \times [0,1]$ at $t = 10$. Only 6948 grid points are required to obtain the error level -2.14, see Fig. 13. To reach the same error level we need 30,824 grid points when using the UFVM.

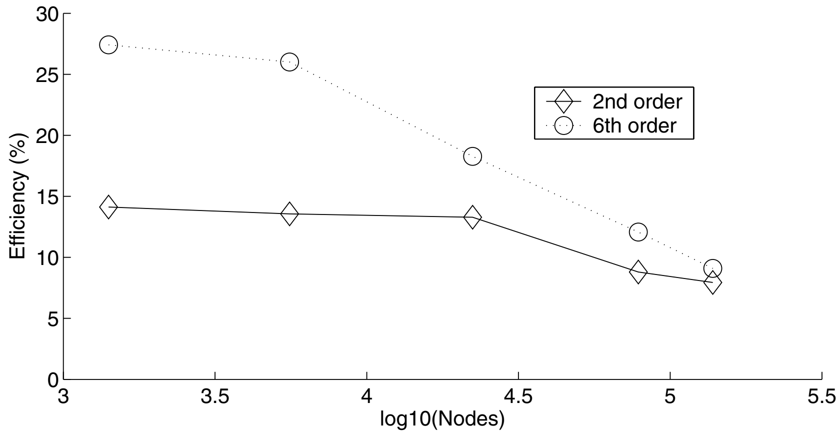

Fig. 11. Estimated efficiency for rightgoing waves, the "source to far field" case.

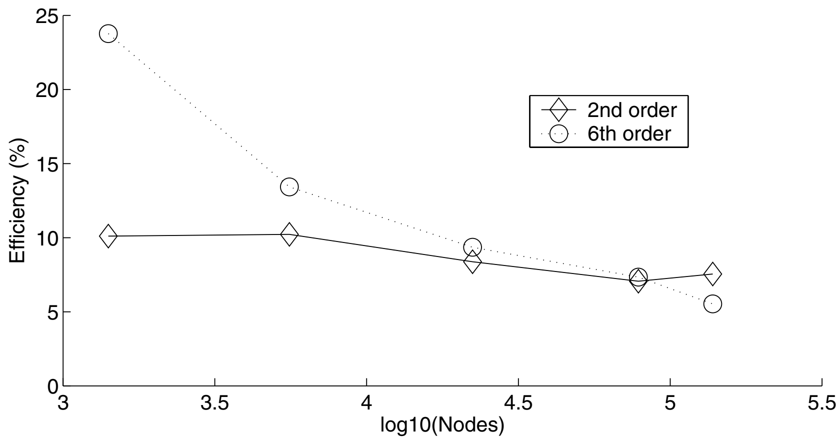

Fig. 12. Estimated efficiency for leftgoing waves, the "far field to source" case.

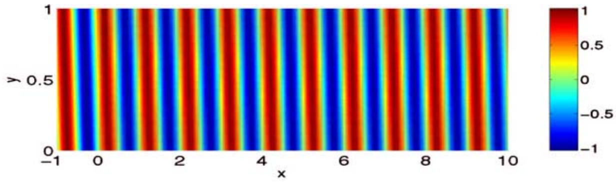

(a) solution at $T = 10$

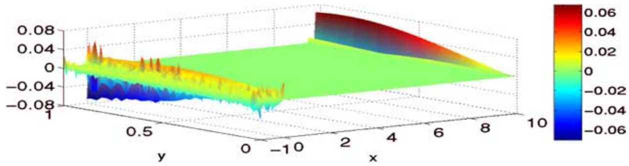

(b) error at $T = 10$

Fig. 13. The total $\log(L_2 - \text{error}) = -2.14$ for $u_t + u_x + 10u_y = 0$. $\log(L_2 - \text{error}) = -2.20$ on the left subdomain $[-1,0]\times[0,1]$ with 2807 nodes and $\log(L_2 - \text{error}) = -2.13$ on the right subdomain $[0,10]\times[0,1]$ with 101×41 nodes.

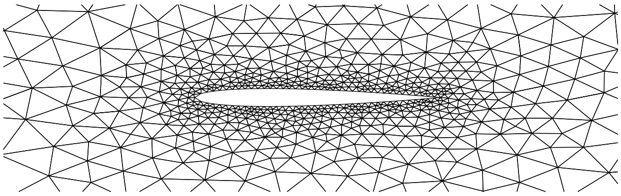

Fig. 14. Unstructured mesh for the airfoil.

3.4. Complex geometry

The UFVM works well on unstructured grids in complex geometries. To illustrate that, we exclude a part of the left subdomain shaped like a $NACA$0012 airfoil with length 0.2. The unstructured mesh easily handles the geometrical complexity, see Fig. 14. To decide whether we have inflow or outflow on the airfoil, we consider the sign of $(a,b)\cdot\hat{n}$. We specify $\mathbf{u}$ on an inflow boundary where $(a,b)\cdot\hat{n} < 0$. Note that the unit outward-pointing normal $\hat{n}$, points *into* the airfoil shaped cut-out. On an outflow boundary where $(a,b)\cdot\hat{n} \geqslant 0$ we do not impose any boundary conditions.

The UFVM is used on the left subdomain while the HOFDM is used on the right. The calculations for waves propagating from the lower-left corner and the lower-right corner are displayed in Figs. 15 and 16, respectively. In both cases, the airfoil shaped cut-out does not introduce a significant amount of error.

4. Extensions to three dimensions and parabolic problems

The hybrid method described in this paper can be extended to three dimensions by interfacing hexahedra from the structured side with pyramids on the unstructured side. Stability is obtained by modifying the corresponding two-dimensional finite volume norm (choose the dual grid properly) to match the two-dimensional finite difference norm.

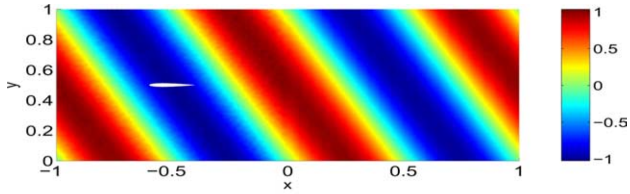

(a) solution at T=1

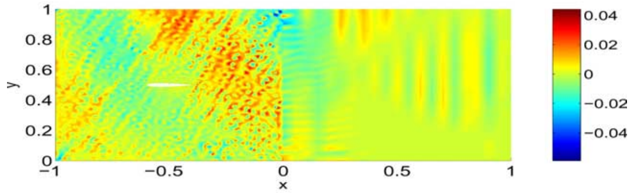

(b) error at $T = 1$

Fig. 15. Waves propagating from lower-left corner. $\log(L_2 - \text{error}) = -1.99$ on the left domain with 3172 nodes and $\log(L_2 - \text{error}) = -2.27$ on the right domain with 861 nodes.

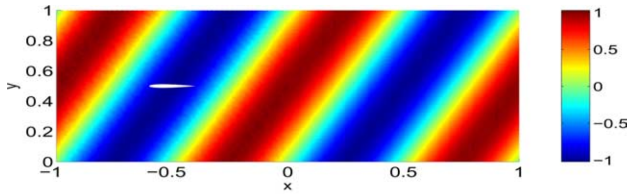

(a) solution at T=1

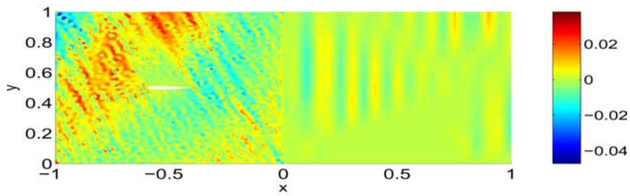

(b) error at $T = 1$

Fig. 16. Waves propagating from lower-right corner. $\log(L_2 - \text{error}) = -1.99$ on the left subdomain with 3172 nodes and $\log(L_2 - \text{error}) = -2.42$ on the right subdomain with 861 nodes.

Parabolic or incompletely parabolic problems (e.g., the Navier–Stokes equations) with second derivatives do not present a major problem for this technique. All the essential steps are in principal included and discussed in this paper. The additional difficulties for parabolic problems are of a more general nature (more complex algebra, additional stiffness, time step limitations, accuracy of penalty terms at the interface, etc.) and are not coupled to this specific procedure.

To maintain uniform accuracy and avoid reflections in the near interface region is very important in many applications. To accomplish that one can adjust the stretching on the structured mesh side, the size of the finite volumes on the unstructured side and the order of accuracy on both sides to arrive at comparable accuracy.

5. Conclusions

A stable hybrid method for hyperbolic problems that combines the unstructured finite volume method with the high-order finite difference method has been developed.

The main tools in the development of the stable interface procedure were the use of SBP operators, weak imposition of interface conditions and the energy method. The stability at the interface was obtained by modifying the dual grid of the unstructured finite volume method close to the interface.

The calculations show that the hybrid method is efficient and accurate. The numerical experiments support that the interface treatment is truly stable.

Extensions to three dimensions and parabolic problems have been discussed.

References

[1] J. Gong, M. Svärd, J. Nordström, Artificial dissipation for strictly stable finite volume methods on unstructured meshes, Computational Mechanics, WCCM VI in conjunction with APCOM'04, September 5–10, Beijing, China, 2004.
[2] M.H. Carpenter, J. Nordström, D. Gottlieb, A stable and conservative interface treatment of arbitrary spatial accuracy, Journal of Computational Physics 148 (1999) 341–346.
[3] K. Mattsson, J. Nordström, Summation by parts operators for finite difference approximations of second derivatives, Journal of Computational Physics 199 (2004) 503–540.
[4] J. Nordström, M.H. Carpenter, High-order finite difference methods, multidimensional linear problems and curvilinear coordinates, Journal of Computational Physics 173 (2001) 149–174.
[5] J. Nordström, R. Gustafsson, High order finite difference approximations of electromagnetic wave propagation close to material discontinuities, Journal of Scientific Computing 18 (2) (2003) 215–234.
[6] J. Nordström, K. Forsberg, C. Adamsson, P. Eliasson, Finite volume, methods unstructured meshes and strict stability, Applied Numerical Mathematics 45 (2003) 453–473.
[7] M. Svärd, J. Nordström, Stability of finite volume approximations for the Laplacian operator on quadrilateral and triangular grids, Applied Numerical Mathematics 51 (2004) 101–125.
[8] M.H. Carpenter, D. Gottlieb, S. Abarbanel, Time-stable boundary conditions for finite-difference schemes solving hyperbolic systems: methodology and application to high-order compact schemes, Journal of Computational Physics 129 (2) (1994).
[9] F. Edelvik, G. Ledfelt, A comparison of time domain hybrid solvers for complex scattering problems, International Journal of Numerical Modeling 15 (5–6) (2002) 475–487.
[10] F. Edelvik, G. Ledfelt, Explicit hybrid time domain solver for the Maxwell equations in 3D, Journal of Scientific Computing 15 (1) (2000) 61–78.
[11] T. Rylander, A. Bondeson, Stable FEM-FDTD hybrid method for Maxwell's equations, Computational Physics Communication 125 (2000) 75–82.
[12] G. Ledfelt, Hybrid Time-Domain Methods and Wire Models for Computational Electromagnetics, Ph.D. Thesis, The Royal Institute of Technology, Department of Numerical Analysis and Computer Science, Stockholm, Sweden, 2001.
[13] M. Djordjevicand, B.M. Notaros, Higher order hybrid method of moments-physical optics modeling technique for radiation and scattering from large perfectly conducting surfaces, IEEE Transactions on Antennas and Propagation 53 (2) (2005) 800–813.
[14] A. Burbeau, P. Sagaut, A dynamic p-adaptive discontinuous Galerkin method for viscous flow with shocks, Computers and Fluids 34 (4–5) (2005) 401–417.
[15] X. Ferrieres, J.P. Parmantier, S. Bertuol, A.R. Ruddle, Application of a hybrid finite difference/finite volume method to solve an automotive EMC problem, IEEE Transactions on Electromagnetic Compatibility 46 (4) (2004) 624–634.
[16] A. Monorchio, A.R. Bretones, R. Mittra, G. Manara, R.G. Martin, A hybrid time-domain technique that combines the finite element, finite difference and method of moment techniques to solve complex electromagnetic problems, IEEE Transactions on Antennas and Propagation 52 (10) (2004) 2666–2674.
[17] U. Andersson, Time-Domain Methods for the Maxwell Equations, Ph.D. Thesis, The Royal Institute of Technology, Department of Numerical Analysis and Computer Science, Stockholm, Sweden, 2001.
[18] H.-O. Kreiss, G. Scherer, Finite element and finite difference methods for hyperbolic partial differential equations, in: C. De Boor (Ed.), Mathematical Aspects of Finite Elements in Partial Differential Equation, Academic Press, New York, 1974.
[19] B. Strand, Summation by parts for finite difference approximation for d/dx, Journal of Computational Physics 110 (1) (1994) 47–67.
[20] J. Nordström, M.H. Carpenter, Boundary and interface conditions for high order finite difference methods applied to the Euler and Navier–Stokes equations, Journal of Computational Physics 148 (1999) 621–645.

[21] B. Gustafsson, The convergence rate for difference approximation to mixed initial boundary value problems, Mathematics of Computation 29 (1975).
[22] B. Gustafsson, The convergence rate for difference approximation to general mixed initial boundary value problems, SIAM Journal on Numerical Analysis 18 (2) (1981) 179–190.
[23] S. Abarbanel, A. Ditkowski, B. Gustafsson, On error bounds of finite difference approximations to partial differential equations – temporal behavior and rate of convergence, Journal of Scientific Computing 15 (1) (2000) 79–116.